NANO · MICRO small
www.small-journal.com

Li-Ion Cooperative Migration and Oxy-Sulfide Synergistic Effect in $Li_{14}P_2Ge_2S_{16-6x}O_x$ Solid-State-Electrolyte Enables Extraordinary Conductivity and High Stability

Bingkai Zhang, Mouyi Weng, Zhan Lin, Yancong Feng, Luyi Yang, Lin-Wang Wang,* and Feng Pan**

Critical to the development of all-solid-state lithium-ion batteries technology are novel solid-state electrolytes with high ionic conductivity and robust stability under inorganic solid-electrolyte operating conditions. Herein, by using density functional theory and molecular dynamics, a mixed oxygen-sulfur-based Li-superionic conductor is screened out from the local chemical structure of β-Li_3PS_4 to discover novel $Li_{14}P_2Ge_2S_8O_8$ (LPGSO) with high ionic conductivity and high stability under thermal, moist, and electrochemical conditions, which causes oxygenation at specific sites to improve the stability and selective sulfuration to provide an O-S mixed path by Li-S/O structure units with coordination number between 3 and 4 for fast Li-cooperative conduction. Furthermore, LPGSO exhibits a quasi-isotropic 3D Li-ion cooperative diffusion with a lesser migration barrier (≈0.19 eV) compared to its sulfide-analog $Li_{14}P_2Ge_2S_{16}$. The theoretical ionic conductivity of this conductor at room temperature is as high as ≈30.0 mS cm^{-1}, which is among the best in current solid-state electrolytes. Such an oxy-sulfide synergistic effect and Li-ion cooperative migration mechanism would enable the engineering of next-generation electrolyte materials with desirable safety and high ionic conductivity, for possible application in the near future.

1. Introduction

Replacing liquid organic electrolytes with inorganic solid-electrolytes (ISEs) in Li-ion battery enables the use of lithium metal anode to markedly boost energy density while increases battery safety.[1–7] For ISEs, chemical/electrochemical stability and Li-ion conductivity of ISEs are the two main factors hindering their development.[8–10] For instance, Li-ion conductivities in the vast majority of reported ISEs are below that of liquid electrolytes such as ethylene/dimethyl carbonate with 1 M $LiPF_6$ (≈10 mS cm^{-1}), and most of ISEs react with negative/positive electrode materials. Therefore, it is not straightforward to obtain ideal ISEs with the most conductivity and stability in order to meet the requirements of all-solid-state Li-ion batteries.

In the past decades, major advances in ISEs are achieved by trial and error, requiring time-consuming experiments and expensive screening of many potential candidates.[11,12] An effective general method for trial and error is to dope isovalent or aliovalent cation/anion in given structural families.[13–16] One example is the LISICON-like structure with the general formula Li_3AX_4, such as β-Li_3PS_4 (LPS), where adjusting the valence of the A and X leads to different structures such as $Li_{3+x}(P_{1-x}M_x)X_4$ (M = Ge, Si, Sn; X = O, S, and Se).[11,14,17–21] However, how to increase the mobility in $Li_{3+x}(P_{1-x}M_x)X_4$ framework while simultaneously to enhance stability is a big challenge. In general, sulfides have very good ionic conductivity but suffer from poor moisture stability and electrochemical

Dr. B. Zhang, Dr. M. Weng, Dr. L. Yang, Prof. F. Pan
School of Advanced Materials
Peking University Shenzhen Graduate School
Shenzhen 518055, China
E-mail: panfeng@pkusz.edu.cn

Dr. B. Zhang, Prof. Z. Lin
School of Chemical Engineering and Light Industry
Guangdong University of Technology
Guangzhou 510006, China
E-mail: zhanlin@gdut.edu.cn

The ORCID identification number(s) for the author(s) of this article can be found under https://doi.org/10.1002/smll.201906374.

Dr. Y. Feng
Guangdong Provincial Key Laboratory of Optical Information Materials and Technology & Institute of Electronic Paper Displays
South China Academy of Advanced Optoelectronics
South China Normal University
Guangzhou 510006, China

Dr. L.-W. Wang
Joint Center for Artificial Photosynthesis and Materials Sciences Division
Lawrence Berkeley National Laboratory
Berkeley, CA 94720, USA
E-mail: lwwang@lbl.gov

DOI: 10.1002/smll.201906374

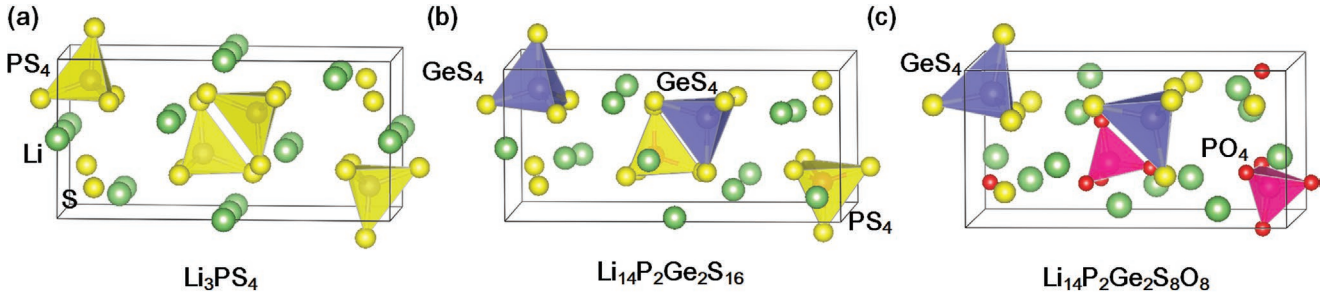

Figure 1. Optimized structure a) β-Li_3PS_4, b) $Li_{14}P_2Ge_2S_{16}$, and c) $Li_{14}P_2Ge_2S_8O_8$. Li (green), S (yellow), O (red), PS_4 tetrahedral (yellow), GeS_4 tetrahedral (blue), and PO_4 tetrahedral (pink).

stability.[19,22–24] On the other hand, oxides, for example, have good stability and reasonably ionic conductivity.[21,25–29] Therefore, it is conceivable that an oxy-sulfide structure contained not one but at least two or three cation/anion, such as PO_4 or GeS_4 units, that blends the best of both the sulfides and oxides into a whole.[26,30] Recent Kato et al. have published a patent about the manufacturing method of crystal oxygen-sulfide solid electrolyte material ($Li_{(4-x)}Si_{(1-x)}P_{(x)}S_{(4-2a)}O_{(2a)}$ (LSiPSO), a=1 − x, $0.65 \le x \le 0.75$).[31] They suggest that more oxygen are imported in crystal LSiPSO structure, as a result, the reducing resistance of LSiPSO against Li foil improves.

Recently, theoretical studies based on density functional theory (DFT) and ab initio molecular dynamics simulation (AIMD) following the procedure in materials project developed by Ceder,[32] Ong,[33–35] and Mo,[36–38] have presented tremendous achievements in the performance of ISEs.[39–41] In this work, by using DFT and AIMD, we have explored a set of $Li_{14}P_2Ge_2S_{16-x}O_x$ composed of structure units, such as $PS_{4-x}O_x$, $GeS_{4-x}O_x$, and $LiS_{4-x}O_x$, and found a stable $Li_{14}P_2Ge_2S_8O_8$ (LPGSO) material that has estimated room temperature conductivity of ≈30 mS cm^{-1} with a low activation energy of ≈0.19 eV. This material also exhibits a wider electrochemical window and small decomposition energy less than 60 meV per atom due to large energy gap between bonding and antibonding bands. Especially, this material shows good water resistance compared to its sulfide-analog. A key feature for high ionic conductivity is distorted tetrahedral or octahedral sites for Li to unfavorably occupy, which creates a smooth energy landscape. We hereby propose an oxy-sulfide framework, and thus, open up a broader scope for structure design toward high-performance ISEs.

2. Results and Discussions

For ISEs, the stability (including phase stability, moisture stability, and electrochemical stability) and ionic conductivity are two main concerns in practice. In the subsequent sections, we first predict the stability of the oxy-sulfide matrix to determine the optimized configuration. Then, we give a comprehensive assessment of Li-ion conductivity by using AIMD simulations. Last, we analyze the Li-ion cooperative migration mechanism in LPGSO. The relationship between structural units and resulting stability and ionic conductivity is also discussed in the following sections.

2.1. The Structure of LPGSO Crystal

The β-Li_3PS_4 crystal structure has an orthorhombic *Pnma* space group in which Li-ions can occupy 4b, 4c, and 8d positions. The composition of $Li_{14}P_2Ge_2S_{16}$ (LPGS) is chosen because this leads to Li interstitials a significant increase in the occupancy of 4c sites. From a structural overview, there are two kinds of non-lithium structure units within LPGS framework, namely PS_4 and GeS_4. These two units build anionic-matrix for Li-ion diffusion and do not share their corner sulfur atoms (S-atoms) with each other. S-atoms belonging to either of them can be partially oxygenated to construct an O-S mixed framework. The typical ground state structure of β-Li_3PS_4, $Li_{14}P_2Ge_2S_{16}$, and $Li_{14}P_2Ge_2S_8O_8$ are shown in **Figure 1**a–c. The lattice constant of LPS, $Li_{14}P_2Ge_2S_{16}$, and $Li_{14}P_2Ge_2S_8O_8$ is shown in **Table 1**. The results from Table 1 suggest that Ge- and O- doping do not change lattice constants obviously.

In terms of the structure, isolated P/GeS_4 tetrahedral units make up the framework of LPGS. Therefore, there are three arrangements for oxygen dopants likely: i) PO_4 units form, all oxygen atoms in the form of PO_4 units, ii) GeO_4 units, all oxygen atoms in the form of GeO_4 units, iii) $PS_{4-x}O_x$ and $GeS_{4-y}O_y$ mixing form. Our approach to predicting stable $Li_{14}P_2Ge_2S_{16-x}O_x$ configuration follows the convex hull like phase diagram in which formation energy for each configuration is determined with respect to $Li_{14}P_2Ge_2S_{16}$ and $Li_{14}P_2Ge_2O_{16}$ as shown in **Figure 2**a. Figure 2a suggests stable configurations lie on the convex hull and oxygenation at PS_4 units is always favored over oxygenation at GeS_4 units. More importantly, for $Li_{14}P_2Ge_2S_{16-x}O_x$ configuration, x = 8 with structural formula $Li_{14}P_2Ge_2S_8O_8$ is the most stable one. This indicates the all PS_4 units are transformed into the PO_4, and further oxygen doping at GeS_4 units is bad for stability. In other words, highly electronegative O^{2-} anions prefer to be bonded with P^{5+} cations to form a PO_4 tetrahedron, leaving Ge^{4+} cations to form a GeS_4

Table 1. Calculated structural parameters for β-Li_3PS_4, $Li_{14}P_2Ge_2S_{16}$, and $Li_{14}P_2Ge_2S_8O_8$ crystal (space group *Pnma*).

	a [Å]	b [Å]	c [Å]	α [°]	β [°]	γ [°]
β-Li_3PS_4	6.25	8.1	13.1	90.0	90.0	90.0
β-Li_3PS_4-Exp.[64]	6.40	8.2	12.2	90.0	90.0	90.0
$Li_{14}P_2Ge_2S_{16}$	6.20	7.8	13.8	89.5	90.0	90.0
$Li_{14}P_2Ge_2S_8O_8$	5.90	7.4	12.1	91.7	90.8	88.9

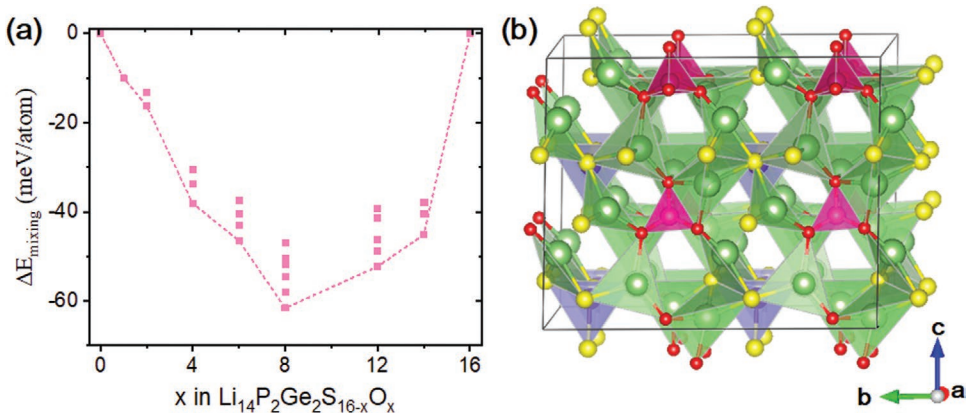

Figure 2. a) Mixing stability (ΔE_{mixing}) in $Li_{14}P_2Ge_2S_{16-x}O_x$ (x ranging from 0 to 12) is shown (reaction equilibrium in Equation (2)). The oxy-sulfide composition ($x = 8$) with formula $Li_{14}P_2Ge_2S_8O_8$ exhibits maximum thermodynamic stability after S–O mixing. Meta-stability upon oxygenation for $8 < x < 12$ is evident from the point above the convex hull. b) Structure of $Li_{14}P_2Ge_2S_8O_8$. Li (green), S (yellow), O (red), GeS_4 tetrahedral (blue), and PS_4 tetrahedral (pink).

tetrahedron. Therefore, $Li_{14}P_2Ge_2S_8O_8$ is the most stable configuration (Figure 2b), which is abbreviated as LPGSO.

2.2. The Stability of LPGSO Crystal

2.2.1. Phase and Moisture Stability

The stability related to the thermal decomposition and the moisture reactivity can affect the cohesiveness of $Li_{14}P_2Ge_2S_8O_8$ composition. Therefore, to understand phase stability with respect to possible decomposed systems, we use the grand canonical linear programming (GCLP) in conjunction with DFT and explored the phase diagram of Li-P-Ge-S-O compounds (**Figure 3**a).[42,43] The GCLP writes the decomposition equation from the original multicomponent compound into all possible smaller compounds and seeks the minimum energy solution under the constraint that the coefficients for all the compounds must be positive. We find that $Li_{14}P_2Ge_2S_8O_8$ is stable with respect to both elemental deposition and decomposition. This means $Li_{14}P_2Ge_2S_8O_8$ can avoid a potentially serious phase instability issue of producing the gas phase. Among several combinations, the most favorable case is the decomposition of $Li_{14}P_2Ge_2S_8O_8$ into ternary compounds, Li_3PO_4 and Li_4GeS_4, with decomposition energy of 51 meV per atom, meaning that up to certain energy window $Li_{14}P_2Ge_2S_8O_8$ would decompose into these ternary compounds. However, the extent of phase instability for $Li_{14}P_2Ge_2S_8O_8$ is smaller than that for $Li_{14}P_2Ge_2S_8O_8$ with respect to decomposition into ternary Li_3PO_4 and Li_4GeO_4 (60 meV per atom).[44] More importantly, the decomposition energy of $Li_{14}P_2Ge_2S_8O_8$ is also lower than that of tetragonal-$Li_{10}GeP_2O_{12}$ (67 meV per atom, and tetragonal-$Li_{10}GeP_2O_{12}$ (space group P42/nmc) has totally different phase structure with $Li_{14}P_2Ge_2S_8O_8$) which has been assembled in solid-state cell and has already been proved to prevent phase decomposition.[45] Therefore, the thermodynamic meta-stability and solid-solid phase transform are less problematic for the application of $Li_{14}P_2Ge_2S_8O_8$ due to the high kinetic barrier.

For moisture stability which is a major hurdle for the widespread use of sulfides ISEs, the H_2S generation energy ($\Delta E_{H2S\ generation}$) for $Li_{14}P_2Ge_2S_{16-x}O_x$ is calculated as shown in Figure 3b. The negative value suggests H_2S generation is thermodynamically favorable.

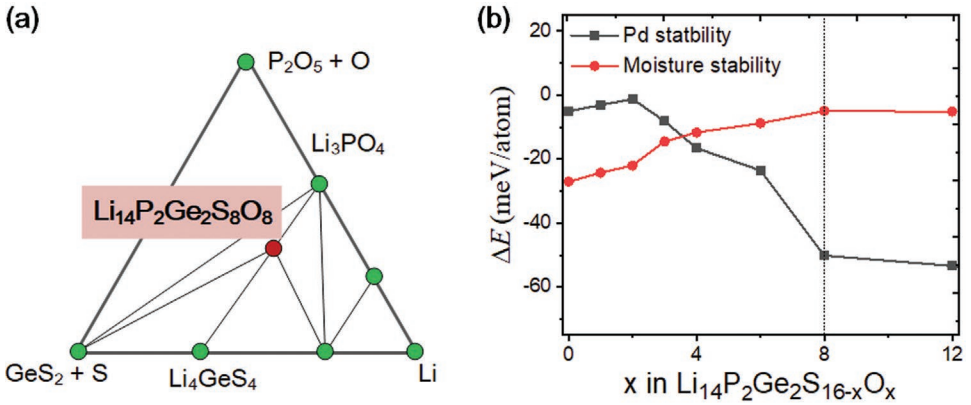

Figure 3. a) Compositions appeared in the Li-P-Ge-S-O phase space along with LPGSO are shown, while the decomposition to ternary phases (Li_3PO_4 and Li_4GeS_4) is the most favorable case. b) Phase decomposition (Pd) stability (ΔE_{Pd}, reaction equilibrium in Equations (3)–(6)) and moisture stability with a gradual increase in O content in the LPGS framework. Oxy-sulfide composition at $x = 8$ exhibits good moisture stability toward water-induced reaction equilibrium in Equation (7).

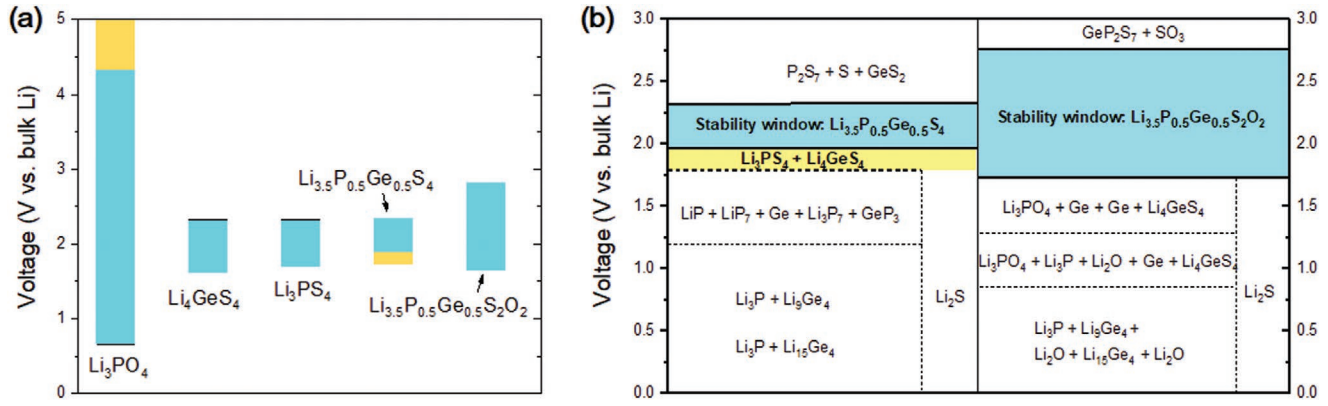

Figure 4. a) Electrochemical stability windows for Li_3PO_4, Li_4GeS_4, Li_3PS_4, LPGS, and LPGSO. b) The voltage profiles and phase equilibria of LPGS and LPGSO upon lithiation and delithiation that determine the anodic and cathodic reactions. The stability window (cyan-shaded region) is determined after the energy consideration of the lithium extraction/insertion without any mixing reactions between the electrode and electrolyte. The yellow region reflects the possible extension of the voltage window over which there is decomposition but without any metallic products.

We find that when $x \geq 8$, $Li_{14}P_2Ge_2S_{16-x}O_x$ is stable with respect to water. Therefore, after the above analysis, LPGSO has both high phase stability and water resistance, and the following calculations are carried out around the LPGSO.

2.2.2. Electrochemical Stability

Following the phase stability and moisture stability, we further examine the electrochemical stability of LPGSO with respect to lithium chemical potential (μL_i). The electrochemical stability windows between LPGSO and other typical ISEs are compared (**Figure 4**a). The results show that that the electrochemical stability of LPGSO outperforms Li_3PS_4, Li_4GeS_4, and LPGS. Meanwhile, LPGSO has the highest cathodic voltage among the sulfides materials. The anodic and cathodic limit for LPGSO is 1.71 and 2.89 V, respectively. Figure 4b shows the equilibrium phases for LPGS and LPGSO. We also note that the phase equilibria for the LPGS at 1.74 V are electron insulator and ion conductor. This decomposition is likely form passivated layer and thus extends the stability window of electrolyte.

To understand the good (phase, moisture, and electrochemical) stability of oxy-sulfides, the project density of states (PDOS) of PS_4 units in LPS, PO_4, and GeS_4 units in LPGSO are shown in **Figure 5**a. The energy difference between the first peaks of bonding and antibonding bands is shown in Figure S1, Supporting Information. As we know oxides tend to have lower energy levels than sulfides, PO_4 unit does have lower anion redox energy level than PS_4 unit in LPS as expected and wider separation (6.9 versus 3.1 eV) between bonding and antibonding states. The PDOS of PO_4 unit is more localized than GeS_4 unit having strong ionic character, hence performing higher stability. GeS_4 unit has similar PDOS states and energy separation (3.0 eV) as PS_4 unit has. All these findings are schematized in Figure S1b, Supporting Information. The deep energy level for PO_4 unit as reflected in ΔE_2 (Figure S1b, Supporting Information) would contribute to LPGSO stability. In summary, we obtain a stable LPGSO configuration with all of PO_4 and GeS_4 units based on Li_3PS_4 and find that LPGSO has good phase stability, moisture stability, and electrochemical stability.

2.3. Li-Ion Conductivity of LPGSO

2.3.1. Dynamic Simulations of LPGSO

To evaluate the Li-ion conductivity of the oxy-sulfide LPGSO, dynamic AIMD simulations are performed over LPGSO and LPGS. Figure 5a shows the Li-ion probability density for LPGSO at 800 K suggests that Li-ions at all sites are involved in diffusion over the 3D pathway. The mean-squared displacement (MSD) also reveals a quasi-isotropic 3D pathway for Li-ion diffusion in LPGS and LPGSO (Figure 5b,c). The calculated Li-ion migration barrier within LPGSO is about 0.19 eV, which is lower than that of LPGS (0.27 eV). Based on the linear fitting of diffusion coefficient (D_{Li}) versus temperature and the Li-ion concentration in LPGSO and LPGS (Figure 5d), the room temperature (298 K) Li-ion conductivity for LPGSO is about 30.0 mS cm^{-1}, which is also larger than that of LPGS (≈13.0 mS cm^{-1}). Therefore, we propose LPGSO as an affordable Li-superionic conductor, which is among the best in current solid electrolytes with ultra-fast Li-ion diffusion.

It is important to ask why the presence of PO_4 or GeS_4 units LPGSO promotes Li-ion conductivity. To this end, we studied the local environment experienced by Li-ion in LPGSO gleaned from radial distribution functions (RDFs) and coordination number, which often provide insight into the long-range (dis) order of the ISEs. **Figure 6**a shows the RDFs and coordination number for Li-S/O interactions calculated over simulation time, and indicate two important features. First, LPGSO (in red) shows weaker peaks of Li-S/O than that in LPGS (in blue) as a reference, indicative of greater disorder. Second, the Li-S/O coordination number for LPGSO shows that Li experiences average coordination between 3 and 4, not only lower than the typical regular tetrahedral sites occupied, for instance, in LPGS, but also far from the NASICON-like and garnet ISEs. The low coordination means an unfavorable or disordered local tetrahedral or octahedral structure, which cannot stabilize Li-ions during migration and thus leads to high conductivity. The strong P–O and Li–O bonding leads to the bond-length distortion for LiS_xO_{4-x} tetrahedra and LiS_yO_{6-y} octahedra. Thus, the oxygen-subsitution in sulfides changes the Li-coordination

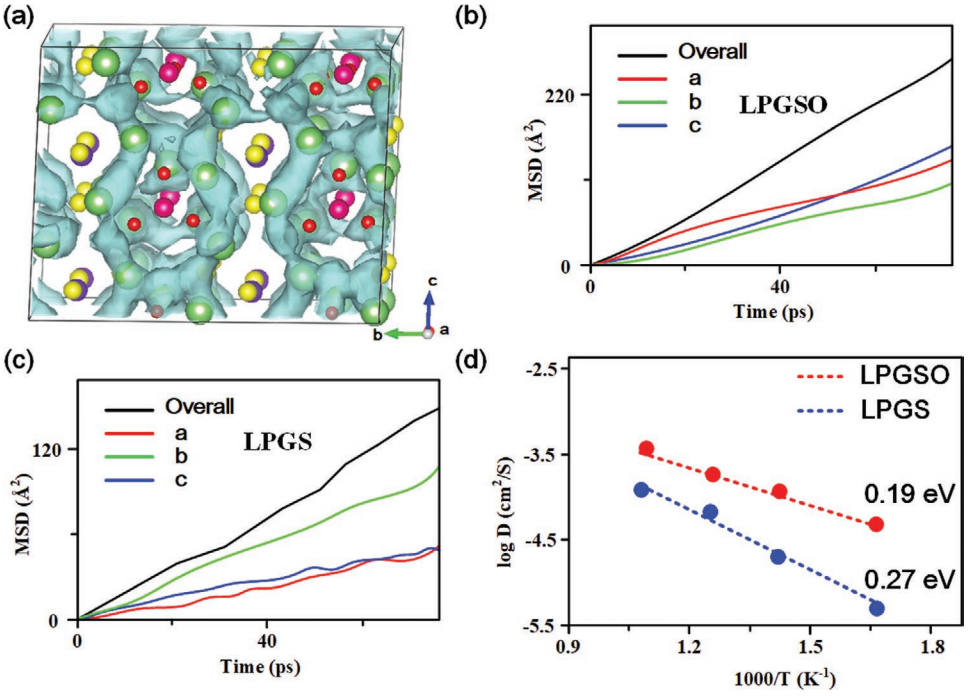

Figure 5. a) Li-ion probability densities (obtained from AIMD simulations at 800 K) in LPGSO shown by the cyan isosurface. b,c) Mean square displacements (MSD) of Li-ions along three different crystallographic directions as well as the overall value obtained from the AIMD trajectory at 800 K within LPGSO and LPGS, respectively. d) Li diffusivity (D) at various temperatures (T) is fitted linearly for LPGSO and LPGS, and corresponding Li-ion migration barriers are given.

environment compared to pure LPGS. Moreover, we suggest that the local geometrical structure sensitivity of Li-ion mobility can be correlated to the tetrahedricity (octahedricity) of $LiS_{4-x}O_x$ ($LiS_{6-x}O_x$) polyhedral. The standard of tetrahedricity (octahedricity) is consistent with previous study, from 100 (perfect tetrahedron (octahedron)) to 0 for a completely distorted one, using the continuous symmetry measures (CSMs) implemented in pymatgen.[46,47] Figure 6b shows a measure of the distortion of Li tetrahedral configuration in LPGSO (red) and LPGS (blue). The distribution of all available sites in LPGSO is at smaller tetrahedricity than LPGS, suggesting highly distorted tetrahedrons in LPGSO. An analysis on octahedral sites leads to a similar conclusion (Figure 6c). LPGSO contains a variety of Li-sites with distorted tetrahedrons or octahedrons, which would provide unfavorable local bonding environments for Li-ion to occupy and thus cause smooth energy landscape.

2.3.2. DFT Computations of LPGSO

To investigate the Li-ion migration mechanisms for LPGSO in detail, DFT calculations combined with the cNEB method are carried out. First, in LPGSO, there are three kinds of Li-ions distinguished by their coordination, namely $Li_{1/1'}$, $Li_{2/2'}$, and $Li_{3/3'}$, as shown in **Figure 7**a. To evaluate the mobility of these Li-ions, we give the statistical analysis of these three Li-ions by calculating the space-time correlation functions $G_s(r, t)$ (Figure S2, Supporting Information). Under 400 K temperature, the defined $G_s(r, t)$ gives the probability that, at the specified time t (1, 10, 20, 30, 40 ps), an atom will be located a distance r away from the location occupied by an atom at an earlier time zero. The detailed introduction is shown in the Supporting Information. For $Li_{2/2'}$-sites, there is only one peak appearing between 0 and 0.6 Å (Figure S2a, Supporting Information).

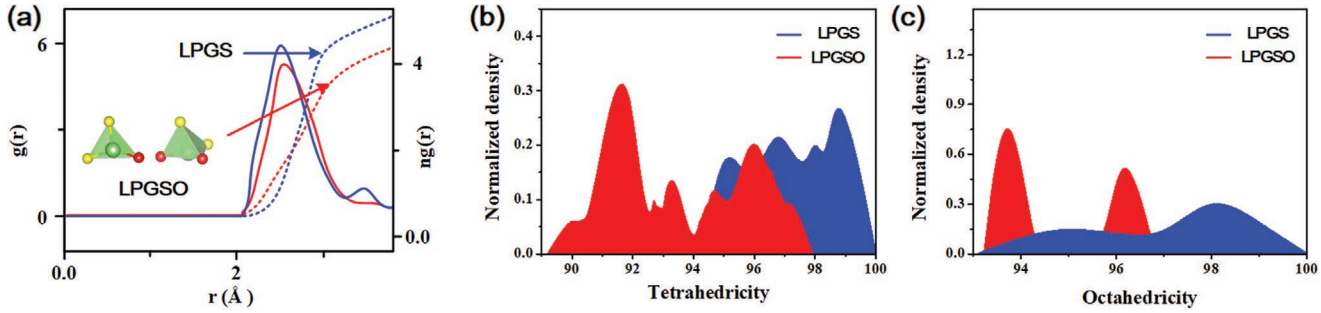

Figure 6. a) Integrated radial pair distribution function and the average number of Li ions at the first coordination sphere of S and O are shown. b,c) Tetrahedral and octahedral sites distortion (tetrahedricity and octahedricity) distribution for the sites occupied by Li-ions in LPGS and LPGSO.

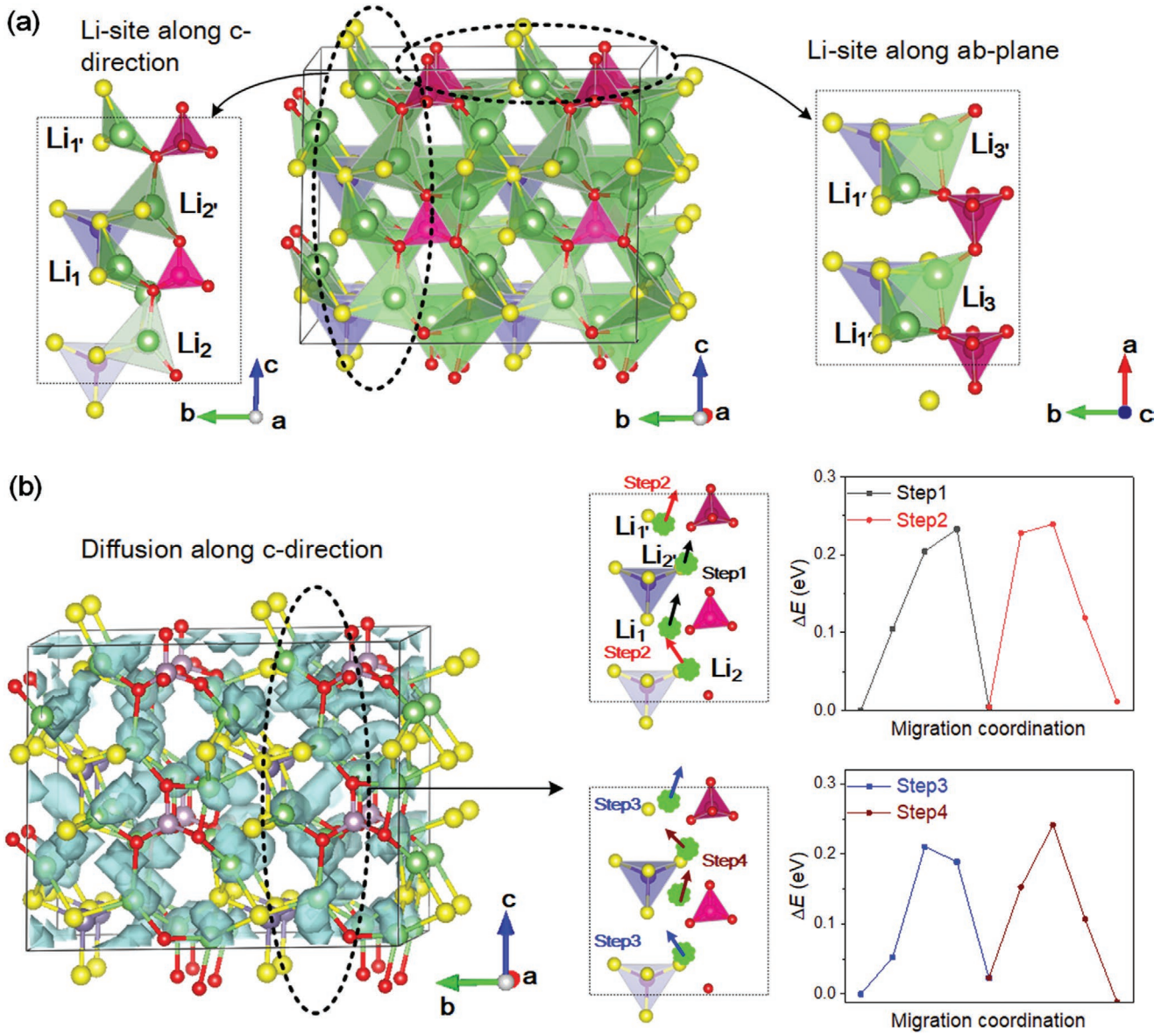

Figure 7. a) The Li-site configuration along c-direction and ab-plane. b) Schematic diagram and energy profile for cooperative migration along c-direction. We separate an overall migration into four steps: step1, step2, step3, and step4. c) Schematic diagram and energy profile for cooperative migration along ab-plane. Li-ion probability densities (obtained from AIMD simulations at 400 K) shown by cyan isosurface. The straight line suggests the migration direction. Green solid spheres represent the Li-ions in LPGSO. Light green, light blue, and pink tetrahedrons represent the LiS_xO_y, GeS_4, and PO_4 tetrahedrons, respectively.

The migration of $Li_{2/2'}$-ion can be considered as a local oscillation within the tedrahedron, suggests high migration barriers around it. For $Li_{1/1'}$-sties, the intensity of the probability peak around 0.6 Å decreases with simulated time (Figure S2b, Supporting Information). This feature suggests that $Li_{1/1'}$-ion displaces its origin positions and jumps to near sites, suggesting low migration barriers around it. Therefore, $Li_{1/1'}$-ions with far more high mobility than $Li_{2/2'}$-ions, they can activate the whole migration.

Recently, cooperative migration in ISEs is widely adopted by the computervision community.[48–52] Two important characteristics of cooperative migration are being the site-energy difference for adjacent Li-ions and being the Li interstitials along Li-ion diffusion pathway. These characteristics have been proposed and researched as principles for achieving cooperative migration by Mo and other researchers.[50,53–55] As for LPGSO, the results from calculated adsorption energy for different Li-ions in LPGSO show that there is a site-energy difference of ≈0.80 eV for adjacent Li-ions, that is, Li_1 and Li_2. On the other hand, Li interstitial migration in isostructural LPS has been reported to follow cooperative mechanism[20] and large Li interstitial concentration in LPGSO. Thus, Li-ion migration in LPGSO can be speculated to follow cooperative mechanism.

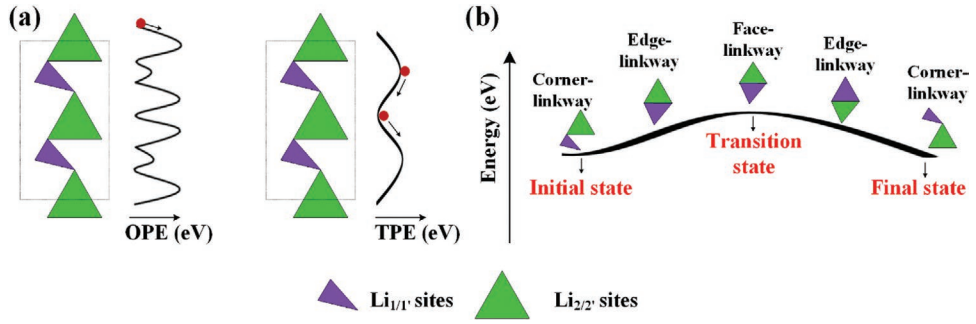

Figure 8. a) A schematic drawing of Li-ion diffusion pathway and their potential energy profiles, one-Li migration potential energy (OPE) and two-Li migration potential energy (TPE). b) The linkway between adjacent polyhedrons along a cooperative migration step. The TPE has more smoothly energy profile based on the theory of Mo et al.[50] The linkway between polyhedrons during cooperative migration changes from corner-, to edge- and to face-shared, and then back again. The initial state and final state keep a corner-linkway of adjacent polyhedrons, intermediates are in an edge-shared way, and transition state with face-linkway is the most unstable one.

Last, for the complex cooperative migration, it is very important to set the local energy minima structure and the migration pathway. To this end, we refer to the snapshot of the lithium trajectory in AIMD simulation. After relaxing the coordination of LiS_xO_y polyhedrons referred from AIMD simulation, we obtain the energy profile of Li-ion migration along *c*-direction and *ab*-plane via the cNEB calculations, as shown in Figure 7b; Figure S3, Supporting Information. The average migration barriers for the process along *b*-direction and *ab*-plane are 0.22 and 0.21 eV, respectively, which is slightly higher than that from AIMD simulation.

After closely inspecting the LiS_xO_y polyhedrons in the intermediates along the Li-ion migration, we find that the facile migration of $Li_{1/1'}$-ion facilitates the neighboring Li-ion to overcome a high-barrier step via forming a metastable structure at which it allows Li-ions to repel one another and smooths the energy profile of Li-ions (**Figure 8**a). In detail, at first the linkage way between $Li(1)S_xO_y$ and $Li(2)S_xO_y$ polyhedrons is corner-sharing, and then the low barrier migration of Li_1-ions leads to the face-sharing linkage ways between them (Figure 8b). According to Pauling's third and fourth rules, the face-sharing polyhedrons are less stable than corner- or edge-sharing ones due to the cation–cation electrostatic repulsion between centroids. Therefore, a key feature for the Li-ion cooperative transport mechanism is the intrinsic low-barrier migration, by which one Li-ion's migration helps another adjacent Li-ion's migration through electrostatic interaction. This transport behavior in LPGSO is very similar to that in tetragonal $Li_{10}MP_2S_{12}$ (M = Si, Ge, and Sn).[16,56]

For cooperative migration, we suggest that it comes from a low-barrier migration step which can lead to a metastable configuration. The low-barrier migration step arises from the edgesharing LiX_4 (X = O or S atoms) tetrahedrons, such as the edgesharing $Li(1)S_4$–$Li(1')S_4$ (dual-Li-sites) in $Li_{10}SiP_2S_{12}$[56] and the edgesharing $Li(3)O_4$–$Li(3)O_4$ structure in $Li_{1+x}Al_xTi_{2-x}(PO_4)_3$.[55] The isolated tetrahedral/octahedral LiX_4 (X = O or S atoms) structure type cannot occur in cooperative migration, such as isolated LiS_4 units in $LiPS_4$ and isolated LiO_6 units in $LiTi_2(PO_4)_3$. Therefore, inserting mobile ions into isolated tetrahedral/octahedral LiX_4 (X = O or S atoms) structure to build edgesharing LiX_4 units is an important strategy, such as aliovalent substitution of non-Li cations with lower valences.

3. Conclusion

The oxy-sulfide LPGSO has been investigated as a solid-state electrolyte via DFT calculation and AIMD in combination with procedures implemented in materials project. We explore the chemistry of local structural in $Li_{14}P_2Ge_2S_{16-x}O_x$ with a mixed framework in order to achieve "advantage complementary" from oxides and sulfides. We identify $Li_{14}P_2Ge_2S_8O_8$ as an oxy-sulfide solid-state electrolyte with enhanced conductivity and stability. This new compound is thermodynamically stable against the decomposition toward its parent quaternary compounds as well as gas-phase binary compounds. This compound exhibits moisture stability against moisture as well as a wide electrochemical stability window compared to its sulfide-analog. The mixture of PO_4 and GeS_4 units offers an unusual crystal structure, which has no regular tetrahedral or octahedral sites for Li-ion to favorably occupy. Consequently, this system results in a quasi-3D Li-ion diffusion path and promotes ionic conductivity significantly (≈30.0 mS cm^{-1}). The current DFT work advance the understanding of the oxygen-sulfide configuration and inspire future work in sulfides for electrolyte applications. For future studies, it is very interesting to use the Kato's producing method to design oxygen–sulfide electrolyte.[31]

Overall, the principle developed from this work indicates that oxygenation at specific sites can improve stability whereas selective sulfuration provides an O–S mixed path for fast Li-conduction. Such synergy would enable search for next-generation electrolyte materials with desirable safety and high ionic conductivity, and engineering them for possible application in the near future.

4. Experimental Section

DFT Methods and Bulk Models: Lattice relaxation was performed using the first-principles calculations as implemented in Vienna initio Simulation Package (VASP) with the projector augment-wave approach (PAW).[57,58] Perdew–Burke–Ernzerhof (PBE) generalized gradient approximation implemented in VASP with a kinetic energy cut-off of 500 eV was used in lattice relaxation.[59] All atomic positions and lattice parameters were allowed to relax until the forces on the atoms were less than 0.01 eV $Å^{-1}$. A k-point grid

of 2 × 2 × 2 was used for a supercell dimension of ≈12 Å × 8 Å × 13 Å. The analysis of Li-ion migration mechanism was calculated by the climbing image nudged elastic band (cNEB) methods.[60] Two local energy minima structures were optimized first, then three initial images were set between them by linear interpolation, and was fully relaxed finally. The adsorption energy of Li-ion was calculated by the following

$$E_{\text{formation}} = E_{\text{perfect}} - E_{\text{defect}} - \mu_{\text{Li-metal}} \tag{1}$$

where E_{perfect} and E_{defect} represent the total energies of the perfect and defected supercells, respectively. $\mu_{\text{Li-metal}}$ is the chemical potential of bulk Li metal.

Phase Stability and Electrochemical Stability: For phase stability, a mixing formation energy (ΔE_{mixing}) of $Li_{14}P_2Ge_2S_{16-x}O_x$ was first calculated with respect to parent quaternary oxide ($Li_{14}P_2Ge_2O_{16}$) and sulfide ($Li_{14}P_2Ge_2S_{16}$) to determine the most stable oxy-sulfide configuration:

$$\Delta E_{\text{mixing}} = \left[E\left(Li_{14}P_2Ge_2S_{16-x}O_x\right) - (16-x)\cdot E\left(Li_{14}P_2Ge_2S_{16}\right) - x\cdot E\left(Li_{14}P_2Ge_2O_{16}\right)\right]/16 \tag{2}$$

Next, the phase decomposition energy (ΔE_{pd}) of $Li_{14}P_2Ge_2S_{16-x}O_x$ was calculated with respect to the most stable ternary compounds (Li_3PS_4, Li_3PO_4, Li_4GeS_4, and Li_4GeO_4) to further check the phase stability. The ΔE_{pd} is defined as follows:

$$\Delta E_{\text{pd}}(x=0) = 2\cdot E\left(Li_3PS_4\right)/4 + 2\cdot E\left(Li_4GeS_4\right) - E\left(Li_{14}P_2Ge_2S_{16}\right) \tag{3}$$

$$\Delta E_{\text{pd}}(0<x<8) = x\cdot E\left(Li_3PO_4\right)/4 + (8-x)\cdot E\left(Li_3PS_4\right)/4 + 2\cdot E\left(Li_4GeS_4\right) - E\left(Li_{14}P_2Ge_2S_{16-x}O_x\right) \tag{4}$$

$$\Delta E_{\text{pd}}(8<x<12) = x\cdot E\left(Li_4GeO_4\right)/4 + (8-x)\cdot E\left(Li_4GeS_4\right)/4 + 2\cdot E\left(Li_3PO_4\right) - E\left(Li_{14}P_2Ge_2S_{16-x}O_x\right) \tag{5}$$

$$\Delta E_{\text{pd}}(x=12) = 2\cdot E\left(Li_3PO_4\right)/4 + 2E\left(Li_4GeO_4\right) - E\left(Li_{14}P_2Ge_2O_{16}\right) \tag{6}$$

According to the above definitions, a negative value means thermodynamic phase stability against decomposition. Last, for moisture stability, H_2S generation energy ($\Delta E_{\text{H2S generation}}$) by considering the reaction equilibrium, M-S + H_2O → M-O + H_2S were calculated. The $\Delta E_{\text{H2S-generation}}$ of $Li_{14}P_2Ge_2S_{16-x}O_x$ is defined as

$$\Delta E_{\text{H2S-generation}} = \left[E\left(Li_{14}P_2Ge_2S_{16-x}O_x\right) - (16-x)\cdot E\left(Li_{14}P_2Ge_2S_{16}\right) - x\cdot E\left(Li_{14}P_2Ge_2O_{16}\right)\right]/16 \tag{7}$$

According to the definition, a positive value means thermodynamic stability against H_2S generation.

For electrochemical stability, reactive equilibria were calculated with respect to lithium chemical potential (μL_i) or grand potential (ϕ) using the grand potential phase diagram approach.[61,62] The ϕ for systems open to Li-ion was determined according to the equation $\varphi(c, \mu L_i) = H(c) - n_{Li}(c)\mu L_i$, in which H(c) is the enthalpy and $n_{Li}(c)$ is the lithium concentration of composition c, and μL_i is the lithium chemical potential. This method was explained in detail in previous work. For any μL_i, the stable composition which lowers the convex hull of ϕ and finally extracts the composition with the lowest energy by a linear combination of these phases was found. Phase diagrams were constructed using the database consisting of DFT computed bulk energies of materials as available in open quantum mechanical database.[42,43] After examining the phase diagram for μL_i ranging from bulk lithium potential (0 V) to the high voltage regime (5 V), the stability window is defined as the voltage window below which the lithium is inserted into the electrolyte and above which the lithium is extracted from these materials yielding the oxidized anion.

Analyzing and Visualizing Trajectories: For Li-ion diffusivity calculations, the AIMD method employing DFT-based force evaluation with a Verlet algorithm to integrate Newton's equations of motion was performed using the VASP software. The NVT (or canonical) ensemble was selected by setting parameters in input file and specifying a Nose–Hoover thermostat. A unit cell containing 136 atoms (16 formula units) and a Γ-point only k-point sampling were chosen for all calculations. The input structure was obtained from the PBE lattice relaxations. The simulation temperature is at 600, 700, 800, and 900 K, and the time step and length of time are 1 fs and 80 ps, respectively. In certain AIMD cases, the length of time and NVT temperature was set in 45 ps and 400 K to check the jump of Li-ions. All analyses were performed using Python Materials Genomics (pymatgen) package and the pymatgen diffusion package developed by Ceder and co-workers.[32,34] The Li-ion diffusion coefficient (D_{Li}) was calculated from the slope of the mean squared displacement (MSD). The room temperature conductivity (σ_{Li}) was also predicted in this work. The calculation details of MSD, D_{Li}, and σ_{Li} are present in the Supporting Information.

For the chemical coordination environment of Li-ion, the ChemEnv tools in pymatgen were used to analyze identify coordination environments that are closest to Li-ion, which included the radial distribution functions (RDFs), coordination number (CN), and continuous symmetry measures (CSMs). RDFs denoted in equations by $g(r)$ define the probability of finding an oxygen/sulfur atom at distance r from another tagged atom. Integrating $g(r)$ in spherical coordinates to the first minimum of the RDFs will give the CN of a Li-ion. Besides the RDFs and CN, identifying the polyhedron based on coordination environments of Li-ions and its distortion degree is also important for ISEs materials. Thus, the CMSs analysis is introduced and helps to determine which model coordination environment (tetrahedron and octahedron are considered in this work) is the closest to the coordination environments of Li-ions. The value of CSMs varies from 0.0 (if a given environment is complete distorted) to 100 (if a given environment is perfect). The distance cutoff (2.62 Å) and angle cutoff (0.3) for Li–X (X = O and S) bonds are set in calculations. More details about CSMs can be found in ref. [46]. In addition, the van Hove correlation function analysis[25,63] is also used in this work, the detailed information are given in the Supporting Information.

Supporting Information

Supporting Information is available from the Wiley Online Library or from the author.

Acknowledgements

This work was supported by National Key R&D Program of China (2016YFB0700600), Soft Science Research Project of Guangdong Province (No. 2017B030301013), Shenzhen Science and Technology Research Grant (ZDSYS201707281026184). Wang was supported by the Assistant Secretary for Energy Efficiency and Renewal Energy of the U.S. Department of Energy under the Battery Materials Research (BMR) program.

Conflict of Interest

The authors declare no conflict of interest.

Keywords

lithium-ion batteries, solid-state batteries, sulfide solid electrolytes, superionic conductors

Received: November 4, 2019
Revised: December 23, 2019
Published online: February 20, 2020

[1] Z. Lin, Z. Liu, N. J. Dudney, C. Liang, *ACS Nano* **2013**, *7*, 2829.
[2] B. Zhang, R. Tan, L. Yang, J. Zheng, K. Zhang, S. Mo, Z. Lin, F. Pan, *Energy Storage Mater.* **2018**, *10*, 139.
[3] C. Sun, J. Liu, Y. Gong, D. P. Wilkinson, J. Zhang, *Nano Energy* **2017**, *33*, 363.
[4] Y. Xiayin, H. Bingxin, Y. Jingyun, P. Gang, H. Zhen, G. Chao, L. Deng, X. Xiaoxiong, *Chin. Phys. B* **2016**, *25*, 018802.
[5] R. Chen, W. Qu, X. Guo, L. Li, F. Wu, *Mater. Horiz.* **2016**, *3*, 487.
[6] Y. Wang, W.-H. Zhong, *ChemElectroChem* **2015**, *2*, 22.
[7] H. Xiang, J. Chen, Z. Li, H. Wang, *J. Power Sources* **2011**, *196*, 8651.
[8] J. Haruyama, K. Sodeyama, Y. Tateyama, *ACS Appl. Mater. Interfaces* **2017**, *9*, 286.
[9] C. Yu, S. Ganapathy, E. R. H. van Eck, H. Wang, S. Basak, Z. Li, M. Wagemaker, *Nat. Commun.* **2017**, *8*, 1086.
[10] J.-S. Kim, W. D. Jung, S. Choi, J.-W. Son, B.-K. Kim, J.-H. Lee, H. Kim, *J. Phys. Chem. Lett.* **2018**, *9*, 5592.
[11] W. D. Richards, Y. Wang, L. J. Miara, J. C. Kim, G. Ceder, *Energy Environ. Sci.* **2016**, *9*, 3272.
[12] T. Famprikis, P. Canepa, J. A. Dawson, M. S. Islam, C. Masquelier, *Nature Mater* **2019**, *18*, 1278.
[13] R. Xiao, H. Li, L. Chen, *Sci. Rep.* **2015**, *5*, 14227.
[14] X. Wang, R. Xiao, H. Li, L. Chen, *Phys. Chem. Chem. Phys.* **2016**, *18*, 21269.
[15] J. C. Bachman, S. Muy, A. Grimaud, H.-H. Chang, N. Pour, S. F. Lux, O. Paschos, F. Maglia, S. Lupart, P. Lamp, L. Giordano, Y. Shao-Horn, *Chem. Rev.* **2016**, *116*, 140.
[16] W. Fitzhugh, F. Wu, L. Ye, W. Deng, P. Qi, X. Li, *Adv. Energy Mater.* **2019**, *9*, 1900807.
[17] Z. Liu, W. Fu, E. A. Payzant, X. Yu, Z. Wu, N. J. Dudney, J. Kiggans, K. Hong, A. J. Rondinone, C. Liang, *J. Am. Chem. Soc.* **2013**, *135*, 975.
[18] N. D. Lepley, N. A. W. Holzwarth, Y. A. Du, *Phys. Rev. B* **2013**, *88*, 2991.
[19] M. Gobet, S. Greenbaum, G. Sahu, C. Liang, *Chem. Mater.* **2014**, *26*, 3558.
[20] Y. Yang, Q. Wu, Y. Cui, Y. Chen, S. Shi, R.-Z. Wang, H. Yan, *ACS Appl. Mater. Interfaces* **2016**, *8*, 25229.
[21] G. Liu, D. Xie, X. Wang, X. Yao, S. Chen, R. Xiao, H. Li, X. Xu, *Energy Storage Mater.* **2019**, *17*, 266.
[22] F. Du, X. Ren, J. Yang, J. Liu, W. Zhang, *J. Phys. Chem. C* **2014**, *118*, 10590.
[23] N. Kamaya, K. Homma, Y. Yamakawa, M. Hirayama, R. Kanno, M. Yonemura, T. Kamiyama, Y. Kato, S. Hama, K. Kawamoto, A. Mitsui, *Nat. Mater.* **2011**, *10*, 682.
[24] N. Adelstein, B. C. Wood, *Chem. Mater.* **2016**, *28*, 7218.
[25] Y. Deng, C. Eames, B. Fleutot, R. David, J.-N. Chotard, E. Suard, C. Masquelier, M. S. Islam, *ACS Appl. Mater. Interfaces* **2017**, *9*, 7050.
[26] K. Takada, M. Osada, N. Ohta, T. Inada, A. Kajiyama, H. Sasaki, S. Kondo, M. Watanabe, T. Sasaki, *Solid State Ionics* **2005**, *176*, 2355.
[27] B. Huang, X. Yao, Z. Huang, Y. Guan, Y. Jin, X. Xu, *J. Power Sources* **2015**, *284*, 206.
[28] Y. Deng, C. Eames, J.-N. Chotard, F. Lalère, V. Seznec, S. Emge, O. Pecher, C. P. Grey, C. Masquelier, M. S. Islam, *J. Am. Chem. Soc.* **2015**, *137*, 9136.
[29] X. Wang, R. Xiao, H. Li, L. Chen, *Phys. Rev. Lett.* **2017**, *118*, 195901.
[30] Y. Sun, K. Suzuki, K. Hara, S. Hori, T.-a. Yano, M. Hara, M. Hirayama, R. Kanno, *J. Power Sources* **2016**, *324*, 798.
[31] R. Kanno, S. Hori, Y. Kato (Tokyo Institute of Technology NUC Toyota Motor Corp.), US. 20180175447A1, **2018**.
[32] S. P. Ong, W. D. Richards, A. Jain, G. Hautier, M. Kocher, S. Cholia, D. Gunter, V. L. Chevrier, K. A. Persson, G. Ceder, *Comput. Mater. Sci.* **2013**, *68*, 314.
[33] S. Chen, J. Yang, C. Ding, R. Li, S. Jin, D. Wang, H. Han, F. Zhang, C. Li, *J. Mater. Chem. A* **2013**, *1*, 5651.
[34] Z. Deng, Z. Zhu, I.-H. Chu, S. P. Ong, *Chem. Mater.* **2017**, *29*, 281.
[35] Z. Zhu, I.-H. Chu, Z. Deng, S. P. Ong, *Chem. Mater.* **2015**, *27*, 8318.
[36] Y. Zhu, X. He, Y. Mo, *J. Mater. Chem. A* **2015**, *4*, 3253.
[37] Y. Mo, S. P. Ong, G. Ceder, *Chem. Mater.* **2012**, *24*, 15.
[38] A. M. Nolan, Y. Zhu, X. He, Q. Bai, Y. Mo, *Joule* **2018**, *2*, 2016.
[39] Y. Yu, Z. Wang, G. Shao, *J. Mater. Chem. A* **2019**, *7*, 21985.
[40] X. Lei, W. Wu, B. Xu, C. Ouyang, K. Huang, *Mater. Des.* **2020**, *185*, 108624.
[41] S. Wang, Q. Bai, A. M. Nolan, Y. Liu, S. Gong, Q. Sun, Y. Mo, *Angew. Chem., Int. Ed.* **2019**, *58*, 8039.
[42] S. Kirklin, J. E. Saal, B. Meredig, A. Thompson, J. W. Doak, M. Aykol, S. Rühl, C. Wolverton, *npj Comput. Mater.* **2015**, *1*, 15010.
[43] S. Banerjee, X. Zhang, L.-W. Wang, *Chem. Mater.* **2019**, *31*, 7265.
[44] S. P. Ong, Y. Mo, W. D. Richards, L. Miara, H. S. Lee, G. Ceder, *Energy Environ. Sci.* **2013**, *6*, 148.
[45] W. Sun, S. T. Dacek, S. P. Ong, G. Hautier, A. Jain, W. D. Richards, A. C. Gamst, K. A. Persson, G. Ceder, *Sci. Adv.* **2016**, *2*, e1600225.
[46] D. Waroquiers, X. Gonze, G.-M. Rignanese, C. Welker-Nieuwoudt, F. Rosowski, M. Göbel, S. Schenk, P. Degelmann, R. André, R. Glaum, G. Hautier, *Chem. Mater.* **2017**, *29*, 8346.
[47] D. Di Stefano, A. Miglio, K. Robeyns, Y. Filinchuk, M. Lechartier, A. Senyshyn, H. Ishida, S. Spannenberger, D. Prutsch, S. Lunghammer, D. Rettenwander, M. Wilkening, B. Roling, Y. Kato, G. Hautier, *Chem* **2019**, *5*, 2450.
[48] S. Shi, P. Lu, Z. Liu, Y. Qi, L. G. Hector, H. Li, S. J. Harris, *J. Am. Chem. Soc.* **2012**, *134*, 15476.
[49] S. Shi, Y. Qi, H. Li, L. G. Hector, *J. Phys. Chem. C* **2013**, *117*, 8579.
[50] X. He, Y. Zhu, Y. Mo, *Nat. Commun.* **2017**, *8*, 15893.
[51] Z. Zhang, Z. Zou, K. Kaup, R. Xiao, S. Shi, M. Avdeev, Y. S. Hu, D. Wang, B. He, H. Li, *Adv. Energy Mater.* **2019**, *9*, 1902373.
[52] Y. Zhao, L. L. Daemen, *J. Am. Chem. Soc.* **2012**, *134*, 15042.
[53] Y. Wang, W. D. Richards, S. P. Ong, L. J. Miara, J. C. Kim, Y. Mo, G. Ceder, *Nat. Mater.* **2015**, *14*, 1026.
[54] X. He, Q. Bai, Y. Liu, A. M. Nolan, C. Ling, Y. Mo, *Adv. Energy Mater.0*, 1902078.
[55] B. Zhang, Z. Lin, H. Dong, L.-W. Wang, F. Pan, *J. Mater. Chem. A* **2020**, *8*, 342.
[56] B. Zhang, L. Yang, L.-W. Wang, F. Pan, *Nano Energy* **2019**.
[57] P. E. Blöchl, *Phys. Rev. B* **1994**, *50*, 17953.
[58] G. Kresse, J. Furthmüller, *Phys. Rev. B* **1996**, *54*, 11169.
[59] J. P. Perdew, K. Burke, M. Ernzerhof, *Phys. Rev. Lett.* **1996**, *77*, 3865.
[60] G. Henkelman, B. P. Uberuaga, H. Jónsson, *J. Chem. Phys.* **2000**, *113*, 9901.
[61] S. P. Ong, L. Wang, B. Kang, G. Ceder, *Chem. Mater.* **2008**, *20*, 1798.
[62] S. P. Ong, A. Jain, G. Hautier, B. Kang, G. Ceder, *Electrochem. Commun.* **2010**, *12*, 427.
[63] S. Adams, R. P. Rao, *J. Mater. Chem.* **2012**, *22*, 1426.
[64] K. Homma, M. Yonemura, T. Kobayashi, M. Nagao, M. Hirayama, R. Kanno, *Solid State Ionics* **2011**, *182*, 53.